Fatigue in Nanometric Single-Crystal Silicon Layers and Beams

Stefano Dellea, Giacomo Langfelder, and Antonio Francesco Longoni

I. Introduction

BULK SINGLE-CRYSTAL and polycrystalline Silicon are brittle materials at room temperature and in ambient conditions, and they do not exhibit susceptibility to static or dynamic fatigue failure during cyclic loading. However, at the micro- and nano-scale, the behavior of Silicon differs from the macro-scale [1]: as early as in 1992, a time-dependent crack growth in a single-crystal Silicon (SCS) beam oscillating at resonance was observed [2]. Nowadays, several micro-electromechanical systems (MEMS) operate at resonance in the kHz to MHz range [3], [4], with a number of loading cycles that easily reaches 10^{11} to 10^{14} in a few years operation. For this reason, MEMS developers need to take into account fatigue as a reliability concern. Although the phenomenology of fatigue in MEMS is well studied, a comprehensive model that can explain all the experimental evidences is still missing. All the suggested theories agree about the marked dependence on the environmental conditions and on the role of surface effects for the lifetime of the tested specimens [5]–[8].

Deepening the knowledge about fatigue in MEMS is thus interesting both from a purely scientific and from an industry-oriented point of view, as the comprehension of the mechanisms generating the failures can improve micro systems reliability.

A way toward this deepening is offered by the constant decrease in the minimum features of MEMS processes: some technologies have already scaled into the NEMS (nano-electromechanical systems) domain, or into combined micro and nano technology (as in the so-called M&NEMS process defined in [9] and [10] and used in this work). NEMS structures offer higher surface-to-volume ratios, lower cross-sections and correspondingly lower critical crack lengths; yet, they typically have a surface morphology (which is at the origin of fatigue) similar to MEMS. Therefore, fatigue phenomena will be likely stronger and/or faster on nano-scale specimens.

The aim of this work is to design and test suitable structures that allow a fatigue analysis in nano-scale single-crystal Silicon specimens, fabricated with a surface micromachining process [10] similar to industrial MEMS technologies. Compared to previous works on fatigue in NEMS [11]–[13], the relatively large number of tested specimens shows a much higher degree of repeatability, making the measurement campaign statistically relevant.

Two different specimens are characterized: the first one is a 250-nm-thick notched layer, directly resembling the geometry of micrometric devices presented in previous works about fatigue [1], [14], [15]. The second one is a 5-μm-long beam with a $(250\ \text{nm})^2$ cross section, resembling nano-gauges used for piezoresistive readout in recent literature works [10], [16]. Both the structures are relevant for the interpretation of the fatigue behavior in silicon due to the increased surface-to-volume ratio with respect to previous works. The second one has also a reliability interest strictly connected to the fabrication of sensors based on piezoresistive nano-gauge readout [9].

The work demonstrates that fatigue occurs earlier in this NEMS specimens with respect to their SCS MEMS counterpart, and puts the obtained data in the context of the theories so far proposed to explain fatigue in MEMS. Clear evidences from the measurement campaign are that:

- during cycles, fatigue is revealed before failure by a slow damage accumulation in both kinds of structures;

- the overall fatigue behavior is well described by a Wöhler curve, with the maximum number of lifecycles decreasing with increasing cycles stress;

- the dependence on the load ratio R (i.e. the ratio of the compressive to the tensile stress, with compression taken as negative), is marked: passing from $R = -0.8$ to $R = -1.2$,

Manuscript received May 28, 2014; revised July 25, 2014; accepted August 13, 2014. The work was supported by the European Union within the FP7-ICT Programme through the NIRVANA Project under Grant 288318. Subject Editor P. M. Sarro.

The authors are with the Department of Electronics, Information, and Bioengineering, Politecnico di Milano, Milan 20133, Italy (e-mail: stefano.dellea@polimi.it; giacomo.langfelder@polimi.it; longoni@elet.polimi.it).

Color versions of one or more of the figures in this paper are available online.

a 10-100 times decrease in the number of lifecycles is observed;

- for the same applied stress, the structure with the smallest cross-section (the nano-gauge), and thus with the smallest critical crack length, shows the shortest fatigue lifetime, and failures within about 10^8 cycles are revealed for stresses as low as 38% of the nominal strength.

II. Theories About Fatigue and Test Devices

In this section, a short review of fatigue theories in Silicon at the microscale is provided. The reader can refer to [5], [7] for a more comprehensive discussion of the phenomena and experimental evidences behind these theories for both SCS and polysilicon. A description of the technology used for the realization of the devices, as well as their structural design, are also given.

A. Scientific Background

According to the scientific literature, several works demonstrated the existence of fatigue in SCS and polysilicon at the microscale [1], [2], [5]–[8], [14], [15], [17]–[22]. The analysis of its dependence on several technological, environmental and operative parameters (e.g. process height, surface roughness, thickness of the native oxide layer; relative humidity, temperature, packaging; static load, dynamic load ratio, load amplitude) has given rise to a debate about the possible physical phenomena that are at the origin of fatigue. Though no theory can comprehensively explain all the observed experimental evidences, two models were given the largest attention: the first one asserts that fatigue originates from the native silicon oxide layer and its thickening under loading conditions [17]. This oxide thickening is favored by the presence of oxygen or water vapor in the environment. The second class of mechanism claims that fatigue damages are mechanically generated from subcritical cracks propagation inside Silicon itself, with wear and debris enforcing their propagation [19]. Key points in favor or against the two models are reported below.

According to the first model, fatigue failures result from a combination of surface oxidation and subcritical crack propagation in the oxide: during loading cycles, the thickness of the native SiO_2 layer can grow up to few times the initial value through stress-assisted oxidation. The stress is also responsible of cracks growth in the SiO_2, and when the crack reaches a critical length, it triggers the final failure. Several findings confirm this model. First of all, the strong dependence from the presence of oxygen and water vapor: the lifetime shortens if the relative humidity increases [6]. Consistently, no fatigue is observed in high vacuum [14], [23], [24]. The stiffness decrease observed in ambient environment before the failure is interpreted as a damage accumulation; no stiffness variations are detected in vacuum. The rate of damage accumulation decreases during the life of the specimen [6], [14], [15], [22]. Finally, the observed increase of the SiO_2 thickness after fatigue cycles is another validating point [17], [21]. Poor initial evidences of static fatigue were in early paper taken as a proof against this model: however recent works markedly showed the existence of static fatigue [25]–[28] with stress

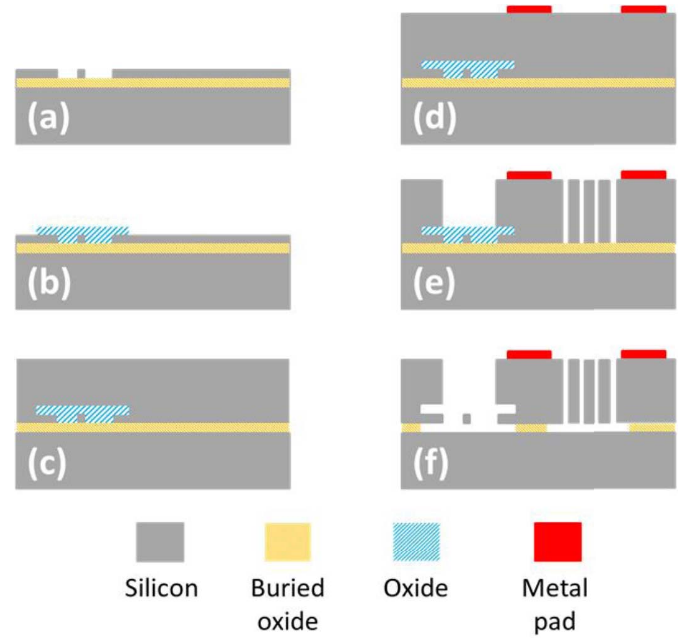

Fig. 1. Schematic representation of the process flow of the technology used for the devices in this work. Starting from an SOI wafer (a) and using common steps like DRIE, DUV and HF attacks (b-f), the process allows designing both micrometric (20 μm thick) and nanometric (250 nm thick) layers.

corrosion cracking occurring clearly in Silicon–even if not as pronounced as in SiO_2. The theory fails to explain the marked role of the compressive portion of the stress.

According to the second model, fatigue is instead a result of crack propagation in the Silicon itself [7], [8], [19]. Roughness, wear, cusps and debris, resulting from the manufacturing of the device or from the cyclic stress, can produce a lever effect inside native surface cracks in Silicon: during the compressive phase of the load, these imperfections can generate a stress amplification at the crack tip, inducing the crack propagation. The model explains the observed strong dependence of fatigue on the compressive stress, as well as the absence of fatigue under constant applied loads. However, the dependence from the environmental conditions is only (weakly) explained by the lower concentration of debris in vacuum. Besides, the quantitative effects of the stress amplification obtainable through this mechanism were reasonably questioned in [20].

Concerning fatigue in SCS at the nano-scale, only a few works were published (see [11]–[13], [29]), but with either a low number of reported samples or a poor initial samples repeatability, which is a relevant parameter for a correct statistical interpretation of fatigue data.

B. Description of the Test Structures

The structures presented in this work were produced at CEA-Leti facilities in Grenoble, France. The process used for the realization of the devices follows the flow sketched in Figure 1 [9], [10]. A 250-nm-thick layer of heavily doped, P-type, single crystal Silicon is grown over a Silicon-on-Insulator (SOI) substrate. The nanometric structures (NEMS) geometry is defined by deep ultraviolet (DUV) lithography

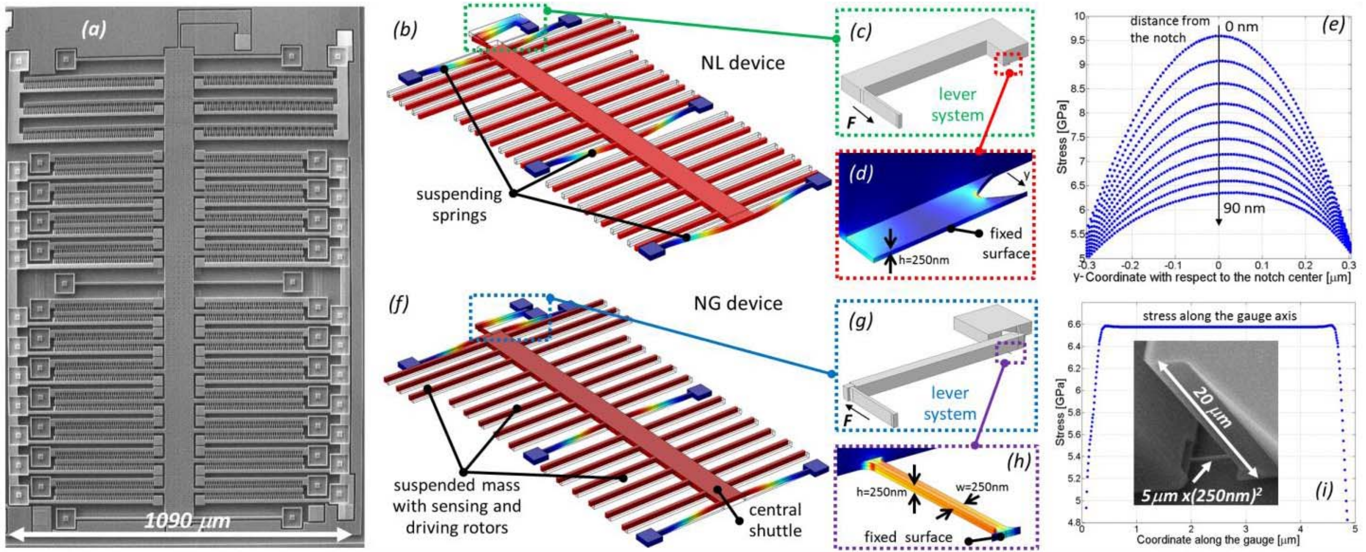

Fig. 2. (a) SEM image of one NL structure (the distortion is due to the microscope); in both structures (b, f) the suspended mass is subject to an electrostatic force generated by comb fingers. The force results in a stress which, through a lever system (c, g) is either concentrated at the notch root of the NEMS layer in the NL device (d), or uniformly distributed along the nano gauge (h). In particular, (e) shows the simulated stress distribution in the notch region of a NL device as a function of the y-distance from the notch center: the 10 different curves refer to cut lines obtained at the intersection of the horizontal plane at 125 nm from the bottom surface and 10 vertical curved surfaces following the notch sidewall profile at increasing distances from the notch; (i) reports the simulated stress distribution along the gauge axis in a NG device (an example of which is captured in the SEM view in the inset). Both (e) and (i) FEM simulations correspond to the critical average failure displacement (see Section III.B).

and reactive ion etching (a). NEMS are then protected with a thin layer (1.3 μm) of oxide. Then, a 20-μm-thick mono- (over the non-protected area) and poly-crystalline (over the protected area) Silicon is grown by epitaxy (c): this structural layer defines a relatively thick movable mass, as in typical surface micromachining processes [14]. Contacts are made by a 0.5 μm metal deposition and etched to create the connection pads (d). MEMS structures are finally defined by deep reactive ion etching (e) and released by hydrofluoric acid vapor etching (f). Fig. 2a is a scanning electron microscope (SEM) image of one realized device.

The operation of both the devices is based on the displacement of a 20-μm-thick, 1.45-mm-long, central shuttle, suspended through six springs (nominal length and width of 291 μm and 7.2 μm respectively). The shuttle is driven by a set of bidirectional comb-finger electrodes (see Fig. 2b-2f). At one end of the seismic shuttle, a lever system is designed, which concentrates the stress onto suitable specimens described below. The shuttle displacement can be monitored via capacitive readout through another set of comb fingers. In particular, the structures have 246 comb fingers with a gap of 1.5 μm for the readout and 1408 comb fingers with a gap of 1 μm for each bidirectional driver. The masses and springs are designed to obtain a natural frequency close to 20 kHz. This value was selected because several MEMS sensors in consumer-grade applications are operated just above the acoustic range, and thus around this value. All high-order modes in both the structures occur, from finite element simulations (FEM), above 40 kHz.

When the actuators apply a force to the central frame in an either positive or negative direction (as in Fig. 2b-2f), its displacement results in an either tensile or compressive stress concentration in a NEMS specimens. Two specimen geometries were designed for fatigue studies:

- the first one (NL) consists in a notched NEMS layer, attached on one side to the MEMS lever system and on the other side to a fixed MEMS anchor point. The NL has a nominal curvature radius of 400 nm at the notch root. The geometry resembles those used in previous works on micrometric specimens [15], and was preliminarily characterized in [1]. The overall device stiffness along the direction of interest is given by both the springs and the lever system (Fig 2c and 2d); in particular, the contribution of the latter is around 5.5% of the overall stiffness. Under an actuation force, the stress distribution concentrates in the notch region and decreases drifting apart from it as detailed in Fig. 2e. From the measurements in [1], the quality factor is in the order of 20 at ambient pressure;
- the second structure (NG) consists in a nano gauge, with a (250 nm)^2 cross-section and a length of 5 μm (Fig 2g and 2h). The beam is linked on one side to a MEMS lever system which well resembles those used in inertial sensors based on this technology [9]. On the other side, it is clamped to an anchored MEMS part. Under an actuation force, the stress distributes almost evenly along the beam axis (Fig. 2i). The contribution of the lever system to the overall stiffness in the direction of the actuator force is around 6.9 %. The expected quality factor is the same as in the NL structure.

For both the devices, the percentage contribution shown above of the levered NEMS specimen to the overall structure stiffness is dictated by a precise need: it was verified in previous works the advantage of having a structure that can be

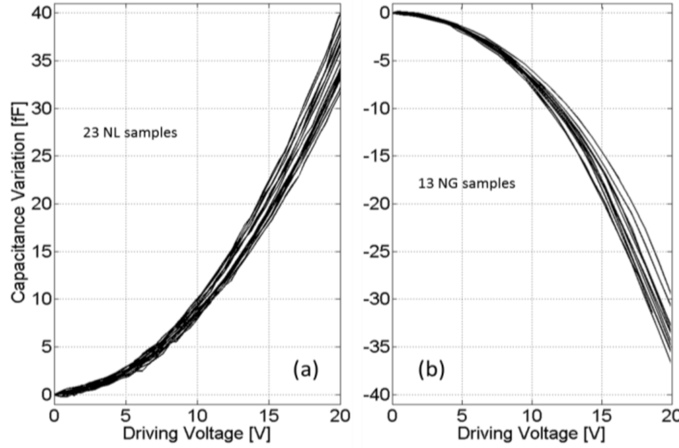

Fig. 3. Collection of quasi-stationary CV curves, obtained on the NL (a) and NG (b) samples. The variance from sample to sample is ascribed to variations in the process height.

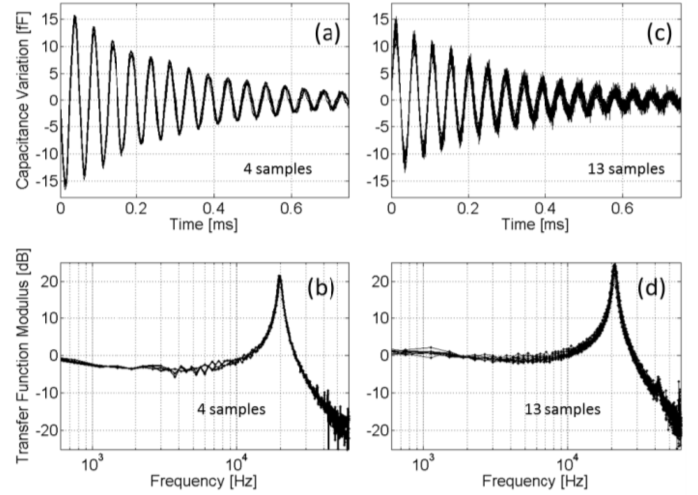

Fig. 4. Collection of dynamic characterization curves (and corresponding FFT) obtained on the NL structures (a and b) and on the NG structures (c and d) for preliminary screening. On average, resonance frequencies $f_{0,NG} = 21.7$ kHz, $f_{0,NL} = 19.8$ kHz and quality factors $Q_{NG} = 18.5$, $Q_{NL} = 19.2$ are found.

led to failure both at resonance (to accelerate fatigue failures) and in a single-cycle (for initial strength evaluation) [15]. Given the maximum voltage (80 V) that can be applied by the instrument used for the characterization (and the corresponding generated electrostatic force), the chosen design guarantees that single-cycle failures can be obtained. In particular, due to the variability of the nominal tensile strength in microscale SCS (with respect to the nominal bulk value of $\sim$7 GPa), the relative stiffness contributions were safely dimensioned in such a way that a voltage of 70 V corresponds to a stress overcoming 11 GPa for both the nano specimens.

III. Electromechanical Characterization

The system used for the measurements campaign is described in details in [30] and [31]. The advantage of this instrumentation is to allow a real time measurement of the devices motion, with good temporal and capacitive resolution [32]. The specimens are tested through a probe station, on a bare wafer in a clean room environment. The temperature change in the entire campaign is in the range of 22 °C–25 °C; the relative humidity is kept reasonably constant (45% $\pm$ 5%) by the clean room conditioning system.

A. Pass/Fail Pre-Screening Procedure

The first part of the tests consists in checking the structures repeatability, to discard devices that deviates significantly from the average behavior. This preliminary check is performed measuring the capacitance-voltage curve (C-V) and the spectral response. The tensile C-V curve is obtained by applying a quasi-stationary voltage ramp on the actuator fingers. The displacement follows a parabolic curve (the electrostatic force being proportional to the square of the voltage). Fig. 3 shows the collection of the prescreening C-V characterization of 23 NL and 13 NG structures. The variance in the C-V curves for the same device type is ascribed to process height variations from part to part on the wafer ($\pm$1.5 μm around a 20 μm thickness). The different concavity of the curves simply reflects the different actuation direction for which a tensile stress is obtained on the NL and NG devices.

Fig. 4a and 4c report the results of the structures response to a downward voltage step [31]. Through an iterative fitting procedure, based on initial guesses found through the FFT of the measured curves (Fig. 4b and 4d), it is possible to precisely evaluate the device resonance frequency and quality factor. On average, these values turn out to be $f_{NG} = 21.7$ kHz, $Q_{NG} = 18.5$, $f_{NL} = 19.8$ kHz, $Q_{NL} = 19.2$ for the NG and NL devices respectively. The limited spread in the resonance frequencies is a further confirmation that the spread in the C-V curves was due to height variations; in a first approximation indeed the resonance is independent on height in such devices.

Over 70 total samples, the devices passing the described procedure were 23 NG samples and 35 NL samples. Part of them was used to estimate the nominal tensile strength (next subsection III.B), while the remainder was used for the fatigue campaign (Section IV).

B. Nominal Strength Evaluation

The second part of the tests consists in evaluating the average NEMS failure voltage and the corresponding stress (i.e. the nominal strength). This step is mandatory to later determine the applied stress (as a percentage of the nominal strength) during fatigue cycles. It is implemented by repeating the C-V procedure up to 70 V, twice consecutively over the sample under test. Since the coefficient of the parabolic C-V curve is related to the overall stiffness of the structure, when the NEMS specimen fails, a sudden stiffness change shifts the characteristic curve on a different parabola. Repeating the measurement after the failure, the new points remain on the new slope. In this way, 12 NL and 11 NG devices are led to failure. Fig. 5 reports examples of single-cycle failures of 4 NL (a-d) and 3 NG (e-g) specimens: note a first stationary curve

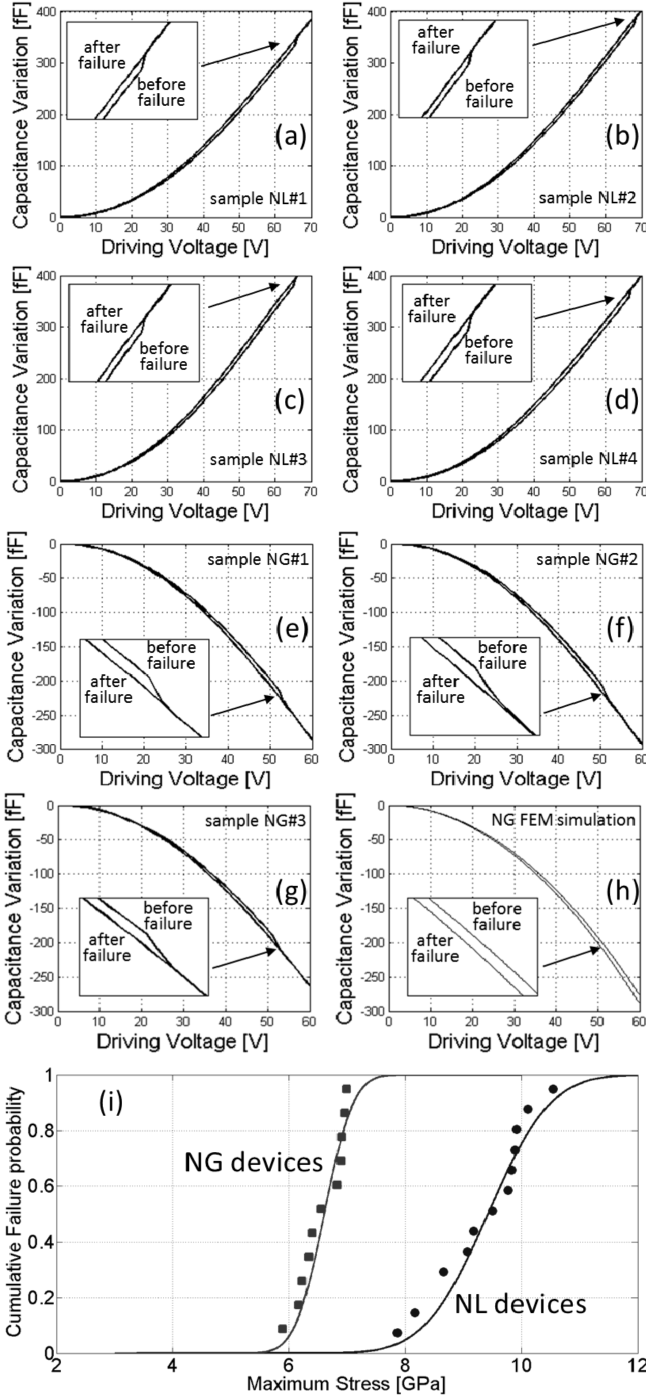

Fig. 5. Examples of C-V curves leading the NEMS specimens to failure. Failure is captured by the sudden change in the device stiffness, which turns into a slope change of the parabola. Plots (a) to (d) refer to NL devices; plots (e) to (g) refer to three NG devices. For comparative purposes, plot (h) reports the results of a FEM simulation of the NG device, with and without the nano-gauge. Finally, (i) reports the cumulative failure probability derived from all the collected data (12 NL devices and 11 NG devices).

(*before* failure) which suddenly shifts onto a steeper slope after the critical voltage is passed. The repetition (*after* failure) lies on the new slope since the beginning, confirming the complete NEMS specimen failure. For comparative purposes, the C-V curve FEM models with and without the NG specimen are shown in Fig. 5h (assuming a 21 μm process height which is within the process corners). On average, the failure voltage found for the NG devices is 51.8 V, with a standard deviation of 1.8 V. For the NL devices, the failure voltage is 66.3 V, with a standard deviation of 2.5 V.

From the knowledge of the average failure voltage and from the device geometry and stiffness, one can estimate the average failure displacement of the central shuttle. This value is then used within a FEM simulator to estimate the corresponding stress on the NEMS specimen, which is its nominal tensile strength. The procedure is described in [33]. The found stresses distributions in the specimens are shown in Fig. 2e and Fig. 2i, showing maximum values of about 9.5 GPa for the NL device (in a position corresponding to the surface and the notch center) and about 6.6 GPa in the NG case (uniform along the beam axis). This lower value is likely due to the larger volume seeing large stresses in the NG device.

All the collected data are used to derive the cumulative failure probability, reported in the Weibull graphs of Fig. 5i.

IV. Fatigue Campaign

The remaining devices are subject to the fatigue tests. The structures, through an automatically increasing sine wave, are led to oscillation up to a chosen (and monitored) maximum displacement. After a fast ramp-up phase (lasting $\sim 10^4$ cycles), the sine amplitude is kept constant. This smooth automatic start-up procedure avoids unwanted failures that may be caused by unwanted overshoots. Only one failure was indeed observed during this start-up procedure.

The tests are performed at a fixed excitation frequency, set 400 Hz below the natural frequency of each device (carefully measured in the characterization phase). As the devices have a bandwidth of $f_0/2Q \sim 560$ Hz, the maximum amplification is guaranteed. Further, as the expected maximum resonance frequency shift before failure is in the order of $\Delta f/f = \frac{1}{2}\Delta k/k \ll 3\%$ ($\ll 600$ Hz), this condition guarantees that during the damage accumulation (i.e. stiffness decrease) the excitation frequency remains within the resonance peak. Therefore, the displacement increase during fatigue can be wholly seen as a stiffness change, rather than caused by the shift of the resonance peak (whose contribution determines a maximum relative stiffness variation $<1/1000$ in the worst case).

A. NEMS Layer Fatigue Results

Operating off-resonance also allows choosing the load ratio, using the bidirectional actuator. Its value is kept around $R = -0.8$ (more tension then compression) for 13 NL devices and around $R = -1.2$ (more compression then tension) for 10 NL devices. The aim is to highlight the role of compression during fatigue cycles, as suggested in [7].

During the test, the device relative stiffness variation is indirectly monitored from the measurement of the relative capacitance variation, which is in turn linear with the relative displacement variation. The test ends after the device failure. Fig. 6a and 6b reports representative examples of monitored relative stiffness changes during fatigue, for two devices

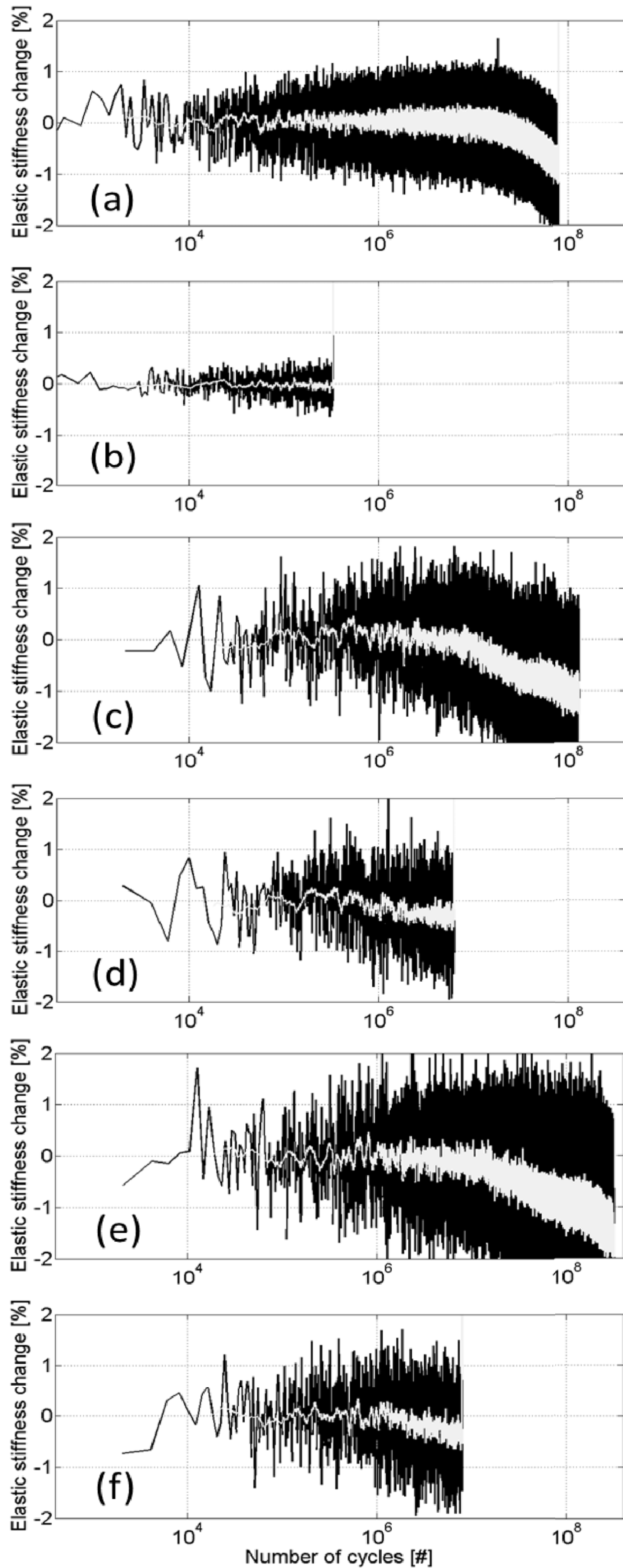

Fig. 6. Representative examples of damage accumulation in the Silicon NEMS layer for 55% (a) and 68% (b) applied stress, and in the Silicon nanogauge for 44% (c), 50% (d), 39% (e) and 48% (f) applied stress. The inner light curve is an average of the outer curve to better highlight the damage accumulation trend.

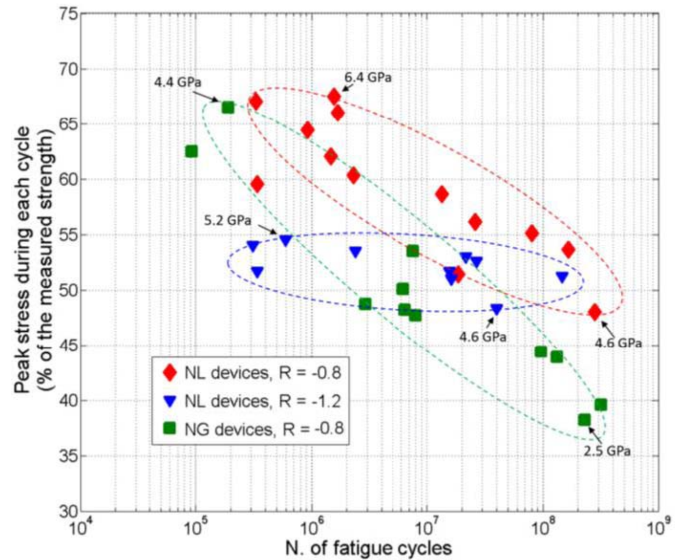

Fig. 7. Overall results of the fatigue tests obtained on NEMS layers (NL) and gauges (NG) in this work. The stress on the y-axis is normalized to the strength measured in the first part of this work. Some absolute stress values are also given by the corresponding numbers, derived from the nominal strength.

surviving about $9{\cdot}10^7$ and $3{\cdot}10^5$ cycles. In the first case, one can appreciate a clear and slow elastic stiffness decrease, which can be ascribed to one of the mechanisms of damage accumulation described in Section 2. Indeed, both subcritical crack propagation and stress-assisted oxidation can be theoretically responsible of stiffness decrease [14]. In the second case, at larger applied stresses, no damage accumulation can be captured by the measuring system and the failure appears suddenly. This indicates a much smaller subcritical crack length at large applied stresses.

At the end of each test, the number of elapsed cycles N is plotted as a function of the peak stress S applied during cycles, in a Wöhler graph. Fig. 7 reports in diamond and triangle markers the results on the NL device at $R = -0.8$ and $R = -1.2$ respectively. Some considerations on these measurements are:

- first, the fatigue resistance is on the whole lower than what observed on most of the experiments performed at the micro-scale on similar specimens and in similar conditions [5], confirming that smaller cross-sections imply higher fatigue failure probability for the same applied stress;
- second, for devices subject to $R = -0.8$, the behavior well matches a Wöhler function $S = N^{-\alpha}$, with $\alpha \sim 0.034$;
- third, for devices subject to $R = -1.2$, the fatigue resistance in the explored N range is lower than above, for the same applied stress (e.g. more than two orders of magnitude lower number of lifecycles at 55% applied stress). Surprisingly, the maximum stress seems rather independent on the number of elapsed cycles, with the points aligning with a very small slope;
- in both cases, failures for stresses lower than 50% of the nominal strength are observed.

As reported and motivated in other works [19], the load ratio, and in particular the compressive portion of the stress, appears to play an important role in the determination of the fatigue phenomenology. Failure may occur during the

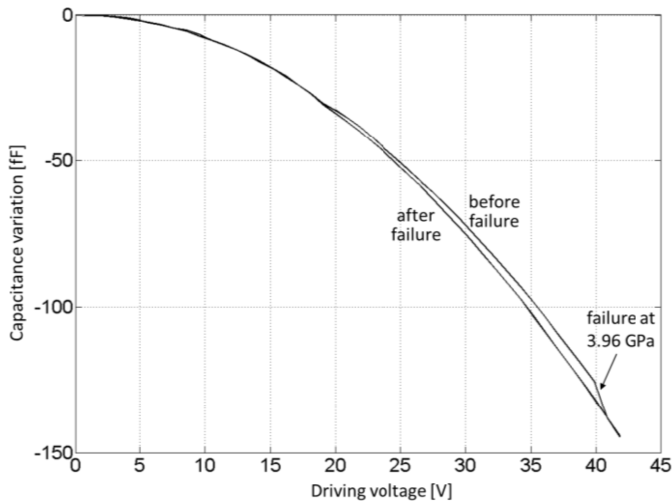

Fig. 8. Single-cycle failure curve for a NG device pre-fatigued at 35% of the nominal strength for $5{\cdot}10^8$ cycles. The failure voltage is 40 V (to be compared with 51.2 V of non-fatigued devices), corresponding to 3.96 GPa (to be compared with 6.6 GPa of non-fatigued devices).

compressive portion of the load, but it was not possible to verify this using the current experimental setup.

B. NEMS Gauges Fatigue Results

Using the same procedure as for the NL devices, 11 NG devices were tested. The load ratio was set to -0.8 as in the case of 13 NL samples. Fig. 6c to 6e report typical results in terms of accumulated damage during fatigue lifetime. On the whole, the behavior is qualitatively similar to what obtained on the NL devices: the maximum accumulated damage is obtained at low stresses and thus for measurements lasting a large number of cycles. In other words, the lower the applied stress, the larger can be the critical crack length.

All the results are again collected in terms of a Wöhler plot in Fig. 7 as square markers. The experimental evidences are the following ones:

- the collected points well align on a Wöhler function $S = N^{-\alpha}$, with $\alpha \sim 0.045$;
- the coefficient of the Wöhler curve is thus larger than for the NL devices, indicating a lower resistance to fatigue cycles for the NG device;
- failures for stresses as low as 38% are observed;
- one further NG device was stopped after $N = 5 \cdot 10^8$ cycles at 35% of the nominal strength, before failure. A single-cycle failure (Fig. 8) was then implemented, which showed a much lower failure stress (3.96 GPa) compared to the nominal strength (6.6 GPa).

Note that (i) samples are on 8" wafers, and it was therefore not possible to significantly tilt them inside the SEM due to the limited available room; and that *(ii)* the NEMS layer lies $\sim$20 μm beneath the Silicon surface, in a cavity surrounded by walls with a relative distance of a few μm. The combination of these issues made practically not possible a SEM analysis to investigate the fracture appearance and propagation directions. This simple aspect should be taken into account for refined designs, to guarantee the possibility of advanced nondestructive microscope inspections.

V. Considerations and Conclusion

The previous Section presented fatigue results for 250-nm-thick Silicon samples with two different geometries. Though the small specimens dimension, compared to the large part of previous studies about fatigue at the microscale, the study presented in this work is quite reliable as the geometry and material repeatability from sample to sample is large, as demonstrated by the preliminary measurements of Section III. Such results confirm the versatility of the designed structures, the effectiveness of the procedure for the characterization and the flexibility of the used electronic system.

There are some experimental evidences about fatigue which are, on the whole, in agreement with previous findings. First, the fatigue lifetime decreases with increasing stresses [34], with a noticeable damage accumulation monitored in terms of elastic stiffness decrease. In particular, the temporal evolution of the measured stiffness decrease appears in agreement with the first model described in Section II [1], [14]. Second, the fatigue behavior seems to accelerate under load ratios lower than -1 (i.e. with a larger compressive than tensile stress), which is usually taken as an evidence supporting the second model described in Section II. The flatness of the Whöler plot obtained in this situation may indicate a contemporary occurrence of strengthening and softening mechanisms, already observed in [5] and [19] at low stresses with large compression. Third, a reduction of the specimen cross-section (as in the NG case with respect to the NL case) determines a lower fatigue lifetime for the same applied stress (as a percentage of the nominal strength). The results in Fig. 7 can be e.g. compared to those obtained on 5-μm-thick samples in [12] where fatigue failures for stresses as low as 40% were obtained after $\sim 10^{10}$ cycles. Here failures for stresses as low as 38% of the strength are obtained after about 10^8 cycles, i.e. two orders of magnitude earlier. Results for SCS under tensile stress in [12] never show failures at stresses lower than 60%. Similar comparisons can be made with other works showing lower fatigue resistance for nano with respect to micro-scale SCS specimens [5]. Failures at even lower stresses on nano-scale specimens were shown in [13], but under bending stress.

Putting these results in the context of the discussed theories about fatigue, on the whole these evidences may lead to the conclusion that the reality is not simply black or white, i.e. there may be the concurrent contribution of more phenomena that can become more or less evident as a function of the testing conditions.

A further conclusion is that the approach suggested in this work – and allowed by this specific process – of extending fatigue studies to sub-micrometric specimens may help in deepening the knowledge about fatigue origin and propagation in structural Silicon used for MEMS and NEMS devices.

In order to further enhance the obtained results, new measurements are planned at different load ratios and in different environmental testing conditions. In particular, one

can exploit more aggressively the bidirectional actuation to reach conditions of either only tensile or only compressive stress. Fatigue measurements under constant applied loads will be as well investigated.

VI. Acknowledgment

The authors acknowledge Ing. J. Della Bosca from Politecnico di Milano for helping with data collection, and P. Rey and A. Berthelot from CEA-Leti for helping with process and design suggestions.

References

[1] G. Langfelder, S. Dellea, P. Rey, A. Berthelot, and A. Longoni, "Investigation of the fatigue origin and propagation in submicrometric silicon piezoresistive layers," in *Proc. IEEE 27th MEMS*, San Francisco, CA, USA, Jan. 2014, pp. 640–643.

[2] J. A. Connally and S. B. Brown, "Slow crack growth in single-crystal silicon," *Science*, vol. 256, no. 5063, pp. 1537–1539, Jun. 1992.

[3] S. E. Alper and T. Akin, "A single-crystal silicon symmetrical and decoupled MEMS gyroscope on an insulating substrate," *J. Microelectromech. Syst.*, vol. 14, no. 4, pp. 707–717, 2005.

[4] L. Mo, V. T. Rouf, M. J. Thompson, and D. A. Horsley, "Three-axis Lorentz-force magnetic sensor for electronic compass applications," *J. Microelectromech. Syst.*, vol. 21, no. 4, pp. 1002–1010, 2012.

[5] D. H. Alsem, O. N. Pierron, E. A. Stach, C. L. Muhlstein, and R. O. Ritchie, "Mechanisms for fatigue of micron-scale silicon structural films," *Adv. Eng. Mater.*, vol. 9, nos. 1–2, pp. 15–30, 2007.

[6] O. N. Pierron and C. L. Muhlstein, "The critical role of environment in fatigue damage accumulation in deep-reactive ion-etched single-crystal silicon structural films," *J. Microelectromech. Syst.*, vol. 15, no. 1, pp. 111–119, Feb. 2006.

[7] H. Kahn, R. Ballarin, and A. H. Heuer, "Dynamic fatigue of silicon," *Current Opinion Solid-State Mater. Sci.*, vol. 8, no. 1, pp. 71–76, Jan. 2004.

[8] H. Kahn, R. Ballarini, J. J. Bellante, and A. H. Heuer, "Fatigue failure in polysilicon not due to simple stress corrosion cracking," *Science*, vol. 298, no. 5596, pp. 1215–1218, Nov. 2002.

[9] A. Walther *et al.*, "3-axis gyroscope with Si nanogage piezo-resistive detection," in *Proc. IEEE 25th MEMS*, Paris, France, Jan. 2012, pp. 480–483.

[10] P. Robert, V. Nguyen, S. Hentz, L. Duraffourg, G. Jourdan, and J. Arcamone, "M&NEMS: A new approach for ultra-low cost 3D inertial sensor," in *Proc. IEEE Sensors Conf.*, Christchurch, New Zealand, Oct. 2009, pp. 963–966.

[11] T. Namuzu and Y. Isono, "High-cycle fatigue damage evaluation for micro-nanoscale single crystal silicon under bending and tensile stressing," in *Proc. 17th IEEE Int. Conf. Micro Electro Mech. Syst. (MEMS)*, Jan. 2004, pp. 149–152.

[12] S. Kamiya *et al.*, "Cross comparison of fatigue lifetime testing on silicon thin film specimens," in *Proc. IEEE 24th Int. Conf. Micro Electro Mech. Syst. (MEMS)*, Jan. 2011, pp. 404–407.

[13] S. Sundararajan and B. Bhushan, "Development of AFM-based techniques to measure mechanical properties of nanoscale structures," *Sens. Actuators A, Phys.*, vol. 101, no. 3, pp. 338–351, Jul. 2002.

[14] G. Langfelder, S. Dellea, F. Zaraga, D. Cucchi, and M. A. Urquia, "The dependence of fatigue in microelectromechanical systems on the environment and the industrial packaging," *IEEE Trans. Ind. Electron.*, vol. 59, no. 12, pp. 4938–4948, Dec. 2012.

[15] G. Langfelder, A. Longoni, and F. Zaraga, "Monitoring fatigue damage growth in polysilicon microstructures under different loading conditions," *Sens. Actuators A, Phys.*, vol. 159, no. 2, pp. 233–240, 2010.

[16] P. E. Allain, A. Bosseboeuf, F. Parrain, S. Maaroufi, P. Coste, and A. Walther, "Large range MEMS motion detection using integrated piezo-resistive silicon nanowire," in *Proc. IEEE 25th Int. Conf. Micro Electro Mech. Syst. (MEMS)*, Paris, France, Jan./Feb. 2012, pp. 1320–1323.

[17] C. L. Muhlstein, E. A. Stach, and R. O. Ritchie, "A reaction-layer mechanism for the delayed failure of micron-scale polycrystalline silicon structural films subjected to high-cycle fatigue loading," *Acta Mater.*, no. 50, no. 14, pp. 3579–3595, Jan. 2002.

[18] S. M. Allameh, P. Shrotriya, A. Butterwick, S. B. Brown, and W. O. Soboyejo, "Surface topography evolution and fatigue fracture in polysilicon MEMS structures," *J. Microelectromech. Syst.*, vol. 12, no. 3, pp. 313–324, Jun. 2003.

[19] H. Kahn, L. Chen, R. Ballarini, and A. Heuer, "Mechanical fatigue of polysilicon: Effects of mean stress and stress amplitude," *Acta Mater.*, vol. 54, no. 3, pp. 667–678, Feb. 2006.

[20] O. N. Pierron and C. L. Muhlstein, "The role of debris-induced cantilever effects in cyclic fatigue of micron-scale silicon films," *Fatigue Fract. Eng. Mater. Struct.*, vol. 30, no. 1, pp. 57–63, Jan. 2007.

[21] D. H. Alsem, C. L. Muhlstein, E. A. Stach, and R. O. Ritchie, "Further considerations on the high-cycle fatigue of micron-scale polycrystalline silicon," *Scripta Mater.*, vol. 59, no. 9, pp. 931–935, 2008.

[22] C. L. Muhlstein, S. B. Brown, and R. O. Ritchie, "High-cycle fatigue and durability of polycrystalline silicon thin films in ambient air," *Sens. Actuators A, Phys.*, vol. 94, no. 3, pp. 177–188, 2001.

[23] V. A. Hong *et al.*, "High-stress fatigue experiments on single crystal silicon in an oxygen-free environment," in *Proc. Solid-State Sens., Actuators, Microsyst. Workshop*, Hilton Head Island, SC, USA, Jun. 2012, pp. 453–456.

[24] M. Budnitzki and O. N. Pierron, "Highly localized surface oxide thickening on polycrystalline silicon thin films during cyclic loading in humid environments," *Acta Mater.*, vol. 57, no. 10, pp. 2944–2955, 2009.

[25] A. Gleizer, G. Peralta, J. R. Kermode, A. De Vita, and D. Sherman, "Dissociative chemisorption of O_2 inducing stress corrosion cracking in silicon crystals," *Phys. Rev. Lett.*, vol. 112, no. 11, p. 115501, Mar. 2014.

[26] A. M. Fitzgerald, R. S. Iyer, R. H. Dauskardt, and T. W. Kenny, "Subcritical crack growth in single-crystal silicon using micromachined specimens," *J. Mater. Res.*, vol. 17, no. 3, pp. 683–692, 2002.

[27] E. D. Renuart, A. M. Fitzgerald, T. W. Kenny, and R. H. Dauskardt, "Fatigue crack growth in micro-machined single-crystal silicon," *J. Mater. Res.*, vol. 19, no. 9, pp. 2635–2640, 2004.

[28] E. K. Baumert, P.-O. Theillet, and O. N. Pierron, "Investigation of the low-cycle fatigue mechanism for micron-scale monocrystalline silicon films," *Acta Mater.*, vol. 58, no. 8, pp. 2854–2863, 2010.

[29] T. Ikehara and T. Tsuchiya, "Low-cycle to ultrahigh-cycle fatigue lifetime measurement of single-crystal-silicon specimens using a microresonator test device," *J. Microelectromech. Syst.*, vol. 21, no. 4, pp. 830–839, Aug. 2012.

[30] C. Buffa, A. Tocchio, and G. Langfelder, "A versatile instrument for the characterization of capacitive micro- and nanoelectromechanical systems," *IEEE Trans. Instrum. Meas.*, vol. 61, no. 7, pp. 2012–2021, Jul. 2012.

[31] ITMEMS. *MEMS Characterization Platform, MCP-A-04, Product Datasheet*. [Online]. Available: http://www.itmems.it, accessed Sep. 2014.

[32] G. Langfelder, A. Tocchio, M. J. Thompson, G. Jaramillo, and D. A. Horsley, "Assessing micromechanical sensor characteristics via optical and electrical metrology," in *Proc. IEEE Sensors Conf.*, Waikaloa, HI, USA, Nov. 2010, pp. 1765–1769.

[33] A. Corigliano, B. de Masi, A. Frangi, C. Comi, A. Villa, and M. Marchi, "Mechanical characterization of polysilicon through on-chip tensile tests," *J. Microelectromech. Syst.*, vol. 13, no. 2, pp. 200–219, Apr. 2004.

[34] T. Straub, P. Theillet, C. Eberl, and O. Pierron, "Comparison of the stress distribution and fatigue behavior of 10- and 25-μm-thick deep-reactive-ion-etched Si kilohertz resonators," *J. Microelectromech. Syst.*, vol. 22, no. 2, pp. 418–429, Apr. 2013.